Mechanical properties of proton conductor ceramics: pristine and fully hydrated

Journal of Power Sources 685 (2026) 240503

Contents lists available at ScienceDirect

Journal of Power Sources

journal homepage: www.elsevier.com/locate/jpowsour

Mechanical properties of proton conductor ceramics: pristine and fully hydrated

Andrea Moranti [a,*], Sandrine Ricote [b], Federico Smeacetto [c], Massimo Santarelli [a]

[a] Department of Energy (DENERG), Politecnico di Torino, Turin, 10129, Italy
[b] Department of Mechanical Engineering, Colorado School of Mines, Golden, CO, 80401, USA
[c] Department of Applied Science and Technology (DISAT), Politecnico di Torino, Turin, 10129, Italy

HIGHLIGHTS

- BZY20 outperforms BCZYYb7111 in elastic modulus, fracture stress, and toughness.
- Hydration weakens BZY20 but strengthens BCZYYb7111.
- SSRS manufacturing boosts BZY20's strength compared to commercial powders.
- 8YSZ tougher, but BZY20 shows promise for scalable protonic ceramic applications.

GRAPHICAL ABSTRACT

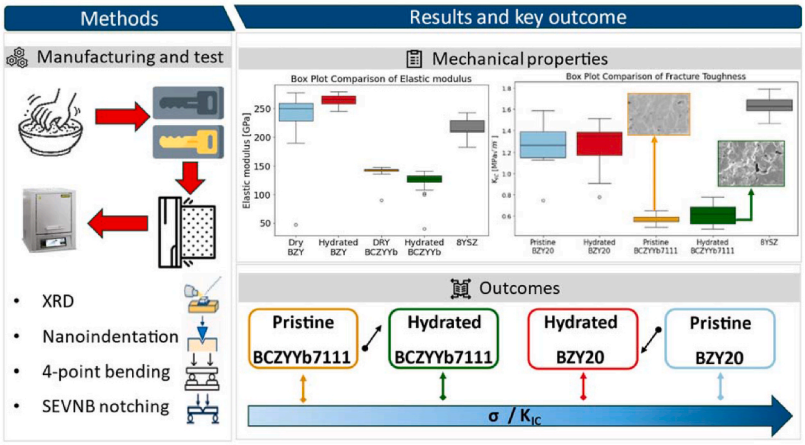

ARTICLE INFO

Keywords:
Protonic ceramics
Mechanical properties
Hydration
Fracture toughness
Elastic modulus

ABSTRACT

Following a literature review to address the existing gaps, this study analyzes the mechanical behavior of the proton-conducting ceramics BZY20 ($BaZr_{0.8}Y_{0.2}O_{3-\delta}$) and BCZYYb7111 ($BaCe_{0.7}Zr_{0.1}Y_{0.1}Yb_{0.1}O_{3-\delta}$), in pristine and fully hydrated states. Key mechanical properties, including elastic modulus, fracture stress, and fracture toughness, are evaluated together with the statistical variability of fracture stress, to assess material reliability and the influence of processing-induced defects. The results highlight distinct mechanical responses between the two compositions with BZY20 exhibiting superior mechanical properties compared to the cerium-rich composition. However, hydration reduces fracture stress and toughness in BZY20, associated with lattice expansion, and a partial shift toward intragranular fracture. In contrast, BCZYYb7111 displays hydration-induced toughening behavior, driven by a transition from predominantly intergranular to intragranular fracture. Overall, these findings suggest that the mechanical performance of proton-conducting ceramics is governed by an interaction between composition, crystal structure, microstructure, and hydration. The results also provide insights for

* Corresponding author.
E-mail address: andrea.moranti@polito.it (A. Moranti).

https://doi.org/10.1016/j.jpowsour.2026.240503
Received 25 March 2026; Received in revised form 8 May 2026; Accepted 22 May 2026
Available online 27 May 2026

mechanically robust protonic ceramics and support the development of durable, scalable materials for long-term energy applications.

1. Introduction

1.1. Protonic ceramic cells

The rising energy consumption, coupled with the goal of reducing greenhouse gas emissions, has driven the adoption of renewable energy sources (RES) as a sustainable alternative. However, the intrinsic intermittency and unpredictability of RES pose challenges for grid stability and energy management. To address these issues, innovative technologies, such as the electrochemical routes, are promising options to balance electricity production, storage, and consumption, also allowing the sustainable production of chemical compounds for hard-to-abate sectors [1].

In this context, protonic ceramic cells (PCCs) have collected significant attention. PCCs are presented as an interesting alternative to solid oxide cells due to their lower operating temperatures (400–600 °C), faster reaction rates, and direct production of dry hydrogen without the need for downstream water separation. Additionally, PCCs exhibit higher theoretical efficiency, reduced Balance of Plant (BoP) requirements, and enhanced resistance to contaminants like H_2S, making them suitable for integration with alternative fuels. However, challenges such as material stability, durability, scalability, and mechanical strength persist, particularly due to their low technological readiness level, which has been tackled in recent years [2].

In the presence of steam, protonic ceramics incorporate protons (or protonic defects) according to the hydration or Stotz Wagner equation, Eq. (1) [3]. Water reacts with oxygen ion vacancies ($v_O^{\cdot\cdot}$) at the surface in the vicinity of neutral oxygen sites ($O_O^{\times}$), forming two protonic defects ($OH_O^{\cdot}$):

$$H_2O + v_O^{\cdot\cdot} + O_O^{\times} \rightleftharpoons 2OH_O^{\cdot} \quad (1)$$

Chemical expansion is observed upon hydration as the protonic defects are larger than the oxygen vacancies they fill [4].

Current research on PCCs focuses on electrolyte material optimization, particularly through doping strategies involving barium cerate ($BaCe_{1-x}M_xO_{3-d}$, M being the dopant) and barium zirconate ($BaZr_{1-x}M_xO_{3-d}$) to adjust conductivity and stability, sintering aids to improve manufacturability, as well as focusing on air electrodes [2,5]. Recent advancements, such as yttrium and ytterbium doping, have enhanced ionic conductivity and sinterability, enabling power densities of up to 1098 mW/cm^2 at 600 °C for more [6] traditional materials and close to 1600 mW/cm^2 for more specifically tuned materials [7], with sensitivity on the gas composition. Nevertheless, technological bottlenecks, such as chemical instability, thermal expansion mismatches, scaling challenges, and the improvement of faradaic efficiency through reduction of electronic leakage, remain critical barriers to commercialization. Despite these complications, PCCs show promising cost-effective hydrogen production, ammonia and methane synthesis, and innovative sensing applications [8–11].

In this work, in order to account these challenges and fill the gap between laboratory performance and industrial deployment, a comprehensive analysis of the mechanical properties of protonic ceramic materials is performed to ensure reliability, durability, and scalability for real-world applications, focusing on investigating the mechanical properties of BZY20 ($BaZr_{0.8}Y_{0.2}O_{3-\delta}$) and BCZYYb7111 ($BaCe_{0.7}Zr_{0.1}Y_{0.1}Yb_{0.1}O_{3-\delta}$), with a particular emphasis on parameters such as elastic modulus, fracture stress, and fracture toughness determined. The results are analyzed using a Weibull distribution, which statistically models the variability in fracture stress data, providing a robust assessment of the materials' reliability and durability throughout the manufacturing process and supporting the development of robust, high-performance protonic ceramic technologies, accelerating their integration into sustainable energy systems and hard-to-abate industrial sectors.

1.2. Literature review and gaps

When surveying the literature, Mercadelli et al. prepared $BaCe_{0.65}Zr_{0.20}Y_{0.15}O_{3-\delta}$-$Ce_{0.8}Gd_{0.2}O_{2-\delta}$ (BCZY–GDC) membranes by tape casting and aged them at 750 °C under different atmospheres (H_2, CO_2, and H_2 + CO_2) [12]. Four-point bending tests at high temperatures, Vickers microhardness, and nanoindentation with a 5 mN peak load were performed. The pristine samples showed a flexural strength of approximately 70 MPa, which decreased after exposure to H_2 due to structural embrittlement and microcracking of the GDC phase (chemical expansion and cerium reduction). On the other hand, CO_2 exposure led to an increase in fracture strength and hardness due to the formation of $BaCO_3$ and Zr-doped ceria (ZDC) phases. When a combination of H_2 and CO_2 atmospheres was employed, only limited mechanical variations were observed, with traces of $BaCO_3$ formation. Overall, the study reported negligible changes in elastic modulus, but the effect of hydration was not assessed.

Hydration and dopant ionic radius effect on the elastic properties of $BaZrO_3$-based materials were considered by Makagon et al. [13]. They studied samples prepared by solid-state reactive sintering and subsequently hydrated in a pure steam atmosphere, following a stepwise temperature decrease to ensure full hydration of the 1–2 mm-thick samples. The number of measurements performed for each case study and hydration level is not specified, with therefore uncertainty on the statistical reliability, but overall hydration shows a slight decrease in the elastic modulus for different $BaY_xZr_{1-x}O_{3-x/2+\delta}H_{2\delta}$, with X = Y, Sc and $0.05 \leq x \leq 0.2$, upon hydration.

In a study from Yang et al., the pristine mechanical properties of $Ba_{1-x}K_xCe_{0\cdot6}Zr_{0\cdot2}Y_{0\cdot2}O_{3-}\delta$ (BKCZY) pellets produced via a citrate–EDTA sol–gel route and pressing, were simply investigated using nanoindentation [14]. The resulting samples exhibited some residual porosity due to volume shrinkage associated with the release of structural water and residual organics. A total of 20 indents per sample were collected to ensure statistical reliability. The effect of dopant concentration and sintering temperature, accounting for the reduced modulus due to larger interatomic distances and Hall-Petch behavior, has been considered. Overall, despite only pristine materials being evaluated (no hydration study), results showed that Ce-containing compositions exhibited lower absolute hardness and modulus values than Zr-rich counterparts.

Theoretical approaches, based on machine learning, show that hydration is supposed to have negative effects on Young's modulus and strength, but are again limited [15].

Different results, due to only partial hydration, have been observed in recent work by Ueno et al., where yttrium-doped barium zirconate ceramics ($BaZr_{0.80}Y_{0.20}O_{3-\delta}$) were subjected to hydration treatments under variable and controlled water vapor partial pressures and durations [16]. Temporary hydration-induced strengthening can be reached due to surface-limited hydration. This can be pointed out by indentation showing hardness values which decrease down to the pristine value when the indentation load is increased. From an electrical perspective, hydration-induced strengthening did not compromise proton conductivity. Similarly, Sažinas et al. reported properties under hydration and dehydration cycles, on samples with three different compositions ($BaZr_{0.80}Y_{0.20}O_{3-\delta}$ (BZY20), $BaZr_{0.90}Y_{0.10}O_{3-\delta}$ (BZY10) and $BaCe_{0.20}Zr_{0.70}Y_{0.10}O_{3-\delta}$ (BZCY721)) produced in this case by solid-state

reactive sintering, with and without sacrificial powder [17]. The specimens were studied using the Vickers micro-indentation technique, despite the inaccurate results of this technique observed for the absolute values being pointed out. Superficial hydration was found to enhance the fracture toughness with a transition from intragranular to intergranular fracture when cerium was present, which was recovered upon dehydration. Overall, the study established that hydration-induced mechanical improvement is reversible, microstructure-dependent, and primarily governed by grain-boundary chemistry rather than bulk lattice expansion.

According to this literature survey, different, and even contradicting, results are observed, with most of the issues found in these studies related to the hydration test protocol: too short hydration dwell time and/or too fast cooling rates do not allow for complete hydration. Therefore, the results are not representative of the operating condition. Another limitation of some of these studies is the limited number of tested samples, which does not provide statistically reliable values.

2. Experimental

2.1. Sample preparation

BZY20 ($BaZr_{0.8}Y_{0.2}O_{3-\delta}$) samples were prepared by two different methods: Solid-State Reactive Sintering (SSRS) and Pechini sol-gel method.

For SSRS, barium carbonate (Alfa Aesar, 99.8 %), zirconium oxide (Alfa Aesar, 99 + % metal basis), and yttrium oxide (Thermo Fisher Scientific, 99.9 %), were milled in ethanol in a jar roller for 24 h with YSZ rod media with a 1:5 wt ratio and then pan dried and manually ground.

For the Pechini sol-gel method, barium nitrate (Sigma-Aldrich, ACS reagent, ≥99%), zirconium(IV) oxynitrate (Sigma- Aldric, technical grade), and yttrium(III) nitrate hexahydrate (Sigma- Aldric, ≥99.8% trace metals basis) were employed. The nitrate precursors were mixed in a distilled water solution and continuously stirred at 60 °C. Citric acid was added to form the complex precursor. 5 min later, ethylene glycol (ThermoScientific) was added and then heated up to 80 °C while keeping it under agitation. When most of the water was evaporated, the solution was heated up at 220 °C in a heater overnight and the product was then ball-milled and calcined at 1100 °C. The powder was ball milled for 24 h and sieved to 200 μm particle size to eliminate the agglomerations of particles on the powder and obtain uniform materials.

$BaCe_{0.7}Zr_{0.1}Y_{0.1}Yb_{0.1}O_{3-\delta}$ (BCZYYb7111) was procured by CerPoTech AS, Trondheim, Norway). In all scenarios, 1%wt NiO (Alfa Aesar, 78.5 % Ni) was used as sintering aid.

The bars for the mechanical tests were prepared using the polymer clay technique: the precursors or fine ceramic powders were mixed with PVA wood glue, mineral oil, and glycerin, with the ratios summarized in Table 1 [18].

The mixed polymeric clay was manually molded and pressed into PVA molds, 3D printed using a commercial Prusa™ printer. The samples, dried in air for a couple days, were sanded to achieve, after sintering, the sizes required by the ASTM C1161−18 standard for Type A samples, consisting in a 25 mm length, 2 mm width and 1.5 mm thickness.

The sintering for all the samples was performed as follows: heating step at 0.7 °C/min from room temperature to 450 °C followed by a dwell of 90 min for debinding and organics burnout, additional heating step at 3 °C/min up to 1550 °C followed by an 8 h dwell, and a final 3 °C/min cooling step down to room temperature. The samples were set on a sintering bed and covered by sacrificial powder of the same composition, to reduce barium depletion.

It is acknowledged that while a sintering temperature of 1550 °C is more appropriate for BZY20, it may be higher than those typically reported for BCZYYb7111 i.e. closer to 1450 °C [19]. However, in this study, identical sintering conditions were employed to enable a direct comparison of the mechanical properties under consistent processing conditions. The potential effects of this choice are discussed in the following results sections.

Table 1
Composition of the polymer clay.

Component	Weight percentage [%]
Solid content	68-73
PVA wood glue	20-25
Mineral oil	3-7
Glycerin	2-5

2.2. Hydration

Half of both BZY20 and BCZYYb7111 rectangular samples was hydrated for comparison with the pristine samples. The hydration was performed with humid gas obtained by flowing N_2 through a heated bubbler to produce 50% humidification with a controlled molar mass composition of 50 mol% H_2O and 50 mol% N_2, corresponding to a water vapor partial pressure of approximately 0.5 atm at atmospheric total pressure. The hydration was performed for 24 h at 600 °C, with heating and cooling steps respectively at 3 °C/min and 0.2 °C/min both under steam. This specific test protocol is expected to guarantee complete hydration. The 24-h dwell at 600 °C is largely superior to the expected transient variation of the defect concentrations of 3-4 h determined in literature [20], and the cooling rate is sufficiently slow to guarantee the hydration at lower temperatures as also performed in other studies [21].

2.3. Drying

After hydration, a drying step was carried out under a dry N_2 atmosphere, using the same thermal profile as the hydration protocol therefore using identical dwell time and heating/cooling rates.

2.4. Thermal cycling treatment

A control treatment was also conducted by applying the same thermal cycle used for hydration, in terms of rates and dwell, while continuously flowing dry N_2 throughout the entire process, therefore reproducing the identical temperature history in the absence of water vapor.

2.5. Materials and mechanical characterization

Some of the sintered bars were ground in a mortar and the powder was analyzed by X-ray powder diffraction (XRD) using $CuK_{\alpha 1}$ radiation recorded with a 2θ between 20° and 80°.

The hardness and reduced elastic modulus were determined via nanoindentation using a diamond indenter (Hysitron TI-950 TriboIndenter). The test protocol consisted of a loading at 2 mN/s up to a maximum of 10 mN, followed by a 2-s dwell before releasing the load. For each sample, 25-30 measurements were carried out, depending on the measurement deviation, and at least 20 measurements per sample were retained after removing outliers.

The reduced modulus is used to assess the elastic one according to the equation:

$$\frac{1}{E_r}=\frac{1-\nu^2}{E}+\frac{1-\nu_i^2}{E_i} \quad (2)$$

with $\nu_i = 0.07$ *and* $E_i = 1141$ *GPa* for the diamond indenter and$\nu = 0.247$ considered from the literature for both materials in both pristine and hydrated form [13].

This measurement was performed on polished samples (to a 0.05 μm finish using a diamond suspension).

Fracture stress and fracture toughness were evaluated with 4-point bend test using a Mark-10 as a loading device and a fixture A (Wyoming Test Fixtures), according to the standards ASTM C1161−18 and to a modified ISO 23146-2008 with samples slightly smaller than the specified ones and consisting of 25 mm length, 2 mm width and 1.5 mm thickness, respectively.

For the fracture stress, at least 30 samples were tested to obtain a Weibull distribution, while for the fracture toughness, a minimum of 5 samples was required to extract the average and standard deviation.

The test protocol for the fracture toughness assessment was identified following a modified ISO 23146-2008 with sample size equal to the ASTM C1161-18.

The fractured surfaces were analyzed using a Scanning Electron Microscope (FEI Quanta 600i Environmental SEM) in high vacuum on gold-coated samples. This analysis was employed to determine the mode of crack propagation, differentiating between inter and intragranular, and to assess the grain size and porosity of the material.

Finally, the sizes and geometric characteristics of the notches were assessed using a digital microscope (Keyence VHX-5000).

2.6. 8YSZ comparison

For all the assessed properties, tests on 8YSZ haven't been experimentally collected by the authors, but several papers from literature have been used [22–31], with approximately 10 references to get statistically reliable values. It should be noted that since the studies were collected from literature, the experimental approaches, starting with manufacturing down to characterization, may differ.

3. Results

3.1. XRD

The diffraction patterns in Fig. 1 show some impurities or secondary phase for the BZY20 samples produced from SSRS, while pure single-phase perovskite structure is obtained for BCZYYb7111. The Ce-rich composition exhibits a shift of the main reflections toward lower 2θ values compared with BZY20, indicating increased d-spacings and, therefore, a larger lattice parameter. This trend is expected because of the lattice expansion upon Ce substitution, as highlighted in the literature for materials with different cerium content [32].

Hydrated BZY20 shows a slight shift towards lower theta after hydration, mostly due to cubic lattice expansion, while the opposite trend is observed for BCZYYb7111. The interpretation of the XRD for BCZYYb7111 is less straightforward due to a distortion-driven expansion or contraction of certain plains [33].

3.2. Nanoindentation and elastic modulus

The Elastic modulus (E), which represents the material's stiffness, was determined for the different materials studied, both in the pristine and hydrated conditions. A higher modulus indicates a stiffer material and therefore smaller strain when the same load or stress is applied, and vice versa.

This mechanical property is strongly related to the microscopic behavior of the material and especially to its atomic level. Elastic strain from the load application, in fact, derives from changes in interatomic distance and related stretch of the bond. Therefore, the value of the elastic modulus reflects the strength of interatomic bonding forces and is proportional to the slope of the interatomic force–distance curve at the equilibrium spacing [34].

The loading and unloading curves obtained in every case study through nanoindentation are represented in Fig. S1 of the Supplementary Information of this work. The few outliers observed can be attributed to the indenter penetrating pores present in the samples, mostly due to organics burnout, and therefore provide measurements that do not accurately represent the material's properties. As 25 to 30 measurements were collected, these outliers could be removed with the criteria of having at least 20 data points for each studied material to get statistically reliable results of the reduced elastic modulus.

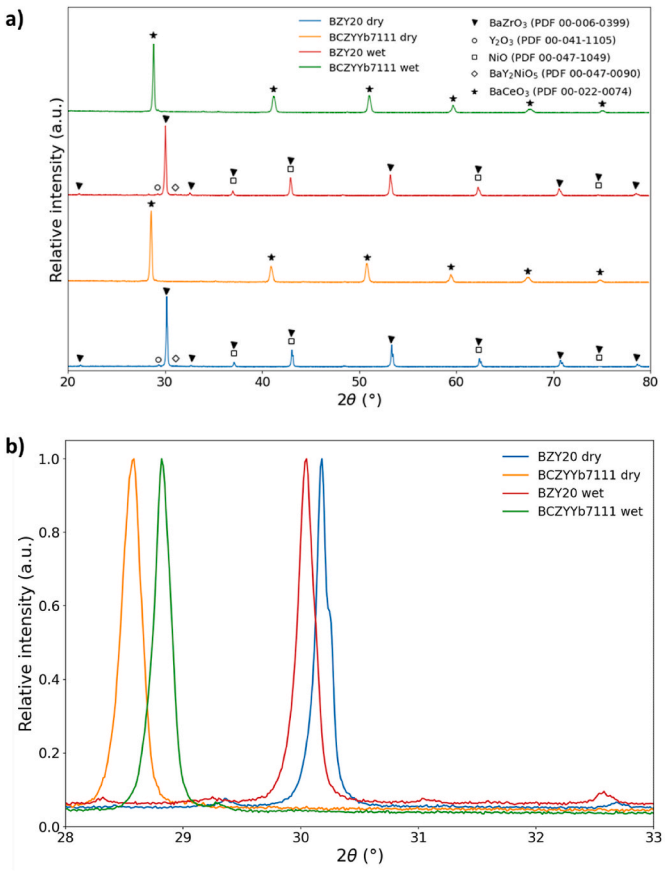

Fig. 1. (a) XRD patterns for BZY20, BCZYYb7111 pristine and hydrated, shifted vertically for clarity, (b) zoomed 28°-32° range to highlight shift.

The reduced elastic modulus derived from these plots could be converted to the Elastic modulus using Equation (1) and is plotted in Fig. 2.

The outliers were removed from the calculations according to the interquartile range method. The slope of the unloading section of the

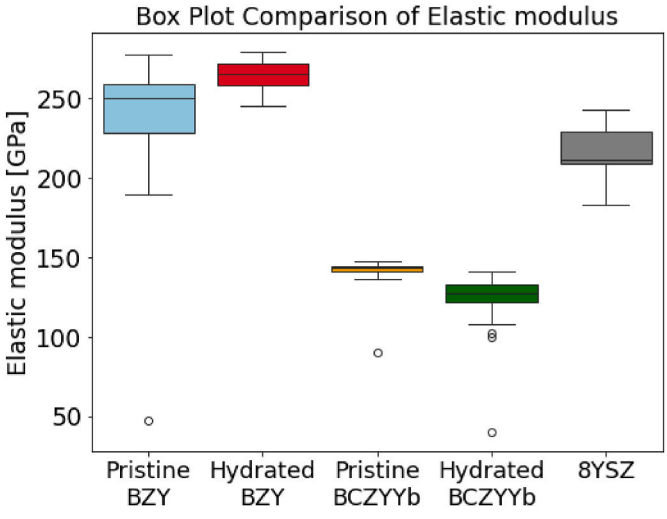

Fig. 2. Elastic modulus box plots comparison.

nanoindentation plots allows the extraction of the hardness of the materials and the elastic moduli, which are summarized in Table 2.

The comparison of these BZY20 and BCZYYb7111 dataset allows us to get an insight into the interaction between the perovskite B-site cations. Firstly, for a coordination number of 6 with oxygen, zirconium (Zr^{4+}) and cerium (Ce^{4+}) exhibit ionic radii respectively of 0.72 Å and 0.87 Å. These values differ from those of yttrium (Y^{3+}), equal to 0.868 Å and ytterbium (Yb^{3+}), of 0.900 Å, which are instead more closely aligned [35].

Increasing the cerium content and substituting half of the yttrium with ytterbium, in BCZYYb7111 is therefore expected to increase the bond length and lattice parameter, supposedly introducing greater structural distortion and weaker overall bonds [14]. In addition to different bond length, adding cerium renders the bond a slightly more ionic (slightly higher electronegativity difference is than with zirconium [36]). As a result, BCZYYb7111 exhibits a more deformed lattice and weaker bonds than BZY20, with a Zr-rich network that is expected to provide greater mechanical properties [17]. As ytterbium and yttrium have similar radii, the effect of substitution is negligible. Regarding electronegativity, instead, ytterbium shows values lower than yttrium and very close to the cerium one, leading therefore again to slightly more ionic bonds. Furthermore, the crystal structure for dry samples is cubic for BZY20 [37] and orthorhombic, or monocyclic, for BCZYYb7111 at low temperatures, such as at room temperature here studied [33,35,38]. After hydration, the cubic structure is expected to remain for BZY20, with a shift in crystal structure for BCZYYb7111 [33]. It should be noted that the bond length in the orthorhombic structure can vary considerably due to increased octahedral tilting [33,39].

In addition to the trend observed when comparing pristine BZY20 and BCZYYb7111, another important assessment concerns the effect of hydration. Several phenomena take place, some leading to improved and others to worsened mechanical properties.

The first effect involves the filling of oxygen vacancies with protonic defects (reaction 1), which restores some missing bonds, resulting in positive effects on the elastic modulus and an increase in stability and lattice reinforcement [13]. Conversely, the introduction of protonic defects lowers the charge from -2e to -1e, weakening the electrostatic bonding and therefore having a negative effect [13]. Another negative impact is associated with the lattice chemical expansion and the corresponding bond weakening. This is caused by the introduction of hydroxyl groups (1.37 Å), which are larger than oxygen vacancies (1.18 Å) [4]. Considering that dehydrated structures contain one oxygen vacancy, while the hydrated structures contain two hydroxyl ions [40], the chemical expansion upon hydration is given by the following equation

$$\beta_{hydr} = 2\beta_{OH_o} - \beta_{V_o} \tag{3}$$

The resultant chemical strain can be expressed as follows:

$$\epsilon_C = \frac{a - a_0}{a_0} \tag{4}$$

and is equal, at 600 °C, to 0.0034 for BZY20 [37] and to 0.00197, with a maximum of 0.00295, for BCZYYb7111 [35].

As found for similar materials in literature [12], elastic modulus variations are minimal, due to a trade-off between the competing effects detailed in the previous paragraph. It is important to point out that the trend is non-unique between BZY20 and BCZYYb7111.

Table 2
Elastic modulus and Hardness for all case studies.

Case study	Elastic modulus [GPa]	Hardness [GPa]
Pristine BZY20	249.4 ± 15.9	11.9 ± 0.5
Hydrated BZY20	264.8 ± 8.0	11.8 ± 0.5
Pristine BCZYYb7111	143.1 ± 2.6	7.5 ± 0.2
Hydrated BCZYYb7111	130.6 ± 5.8	7.3 ± 0.2
8YSZ	215.0 ± 21.1	11.0 ± 1.4

Elastic modulus of dry BZY20 shows, in fact, an increase upon hydration due to the filling of oxygen vacancies with hydroxide ions, which restores missing bonds and reinforces the lattice [13], whereas in BCZYYb7111 the modulus decreases upon hydration. This second result seems to be consistent with the destabilizing effect of multiple dopants, the presence of lattice strain on an asymmetric structure different from the cubic of BZY20, and weaker Ce–O interactions [41]. Hardness values show a similar trend, with BZY20 having higher values in both dry and hydrated form, and BCZYYb7111 significantly lower values, further confirming the remarkable mechanical robustness of Zr-based compositions. These results also suggest a minimal role for hydration on the elastic modulus.

3.3. Fracture stresses and Weibull distributions

If the elastic modulus is a significant indicator of mechanical properties and performance of a material, especially on a microscopic level, the need for a better descriptor of the bulk properties leads to the study of the fracture stress using 4-point bending; it provides accurate absolute macroscopic values also compared to other techniques such as Vickers indentation [16,17]. The tests were performed on at least 30 samples per case study to obtain statistically reliable results.

3.3.1. Pristine BZY20 vs pristine BCZYYb

The Weibull distributions of pristine BZY20 and pristine BCZYYb7111 are shown and compared in Fig. 3, with shape parameters of 2.35 and 2.27, and scale parameters of 63.02 and 22.66, respectively.

The fracture stress of BZY20 is higher than that of BCZYYb7111, consistent with trends observed in the hardness, and it is attributed to differences in intrinsic material properties, processing routes, and microstructural features such as grain size and porosity.

It is also important to note that the BZY20 and BCZYYb7111 bars were prepared using different starting materials. The SSRS route (used for BZY20) was already reported in literature for other perovskite-based ceramics to achieve intrinsically superior mechanical performance [13] and is also confirmed in the following sections of this study. Furthermore, since the precursors' particle sizes used in SSRS are larger, a smaller amount of organics was needed compared to the sub-micron single-phase BCZYYb7111 powder (30 wt% versus 36 wt%). This has a direct effect, especially on the presence of internal pre-cracks and of pores, resulting from the organics burnout [14]. Also, despite the higher porosity of the BCZYYb7111, pores were more homogenously distributed throughout the whole bar, since thinner powder makes mixing easier. Regarding the processing method it should be noted that NiO as sintering aid was also employed, which has been reported to be beneficial for densification and therefore to the mechanical properties [42]. Under certain operating conditions, tough, it may lead to long-term mechanical degradation, particularly through grain-boundary weakening and chemical instability effects [43]. In the present study, the use of a small amount (1 wt%) of NiO is expected to predominantly contribute to densification, with expected limited impact on intrinsic mechanical properties.

Finally, grain size further differentiates the two systems. The lower intrinsic sinterability of BZY20 [13], leads to a finer microstructure due to the presence of Zr, despite the use of SSRS which typically leads to larger grains compared to conventional sintering due to accelerated atomic mobilities [44]. This enhances fracture resistance through Hall–Petch strengthening, whereas the coarser grains of BCZYYb7111 promote crack initiation and propagation, ultimately lowering mechanical robustness [29]. The validity of this effect for ceramic materials has long been discussed in literature: some materials also show a maximum as a function of grain size, especially for non-cubic materials due to microcracking and R-curve effect, with limited or no effect on cubic materials [45]. In contrast, other studies for materials such alumina or zirconia confirm the validity of the Hall-Petch effect [46]. At the same time, this effect is expected to have a lower sensitivity on the

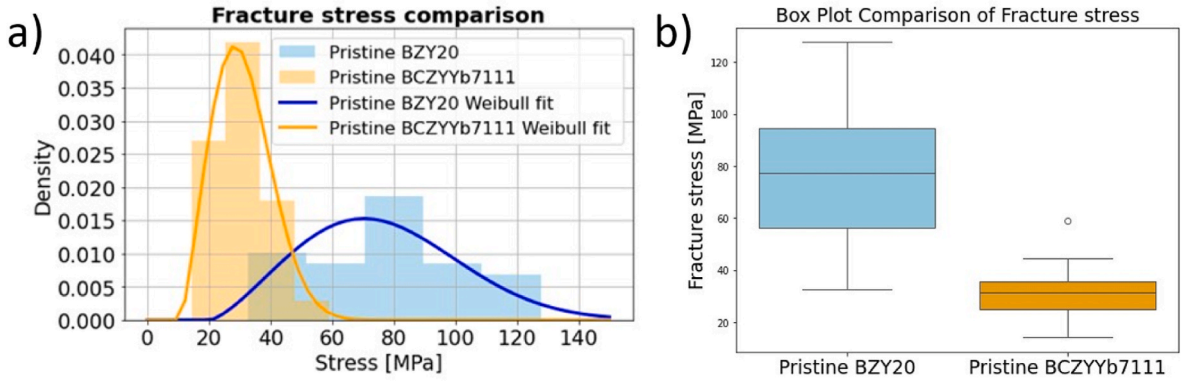

Fig. 3. (a) Weibull distribution and (b) Box Plot of Pristine BZY20 and BCZYYb7111.

mechanical properties with respect to other aspects such us the samples porosity, for which a more detailed focus is carried out in Section 3.5 and is therefore expected to give deeper insights [47].

The more remarkable fracture stress of BZY20 compared to BCZYYb7111 can therefore be justified by two effects: (1) the intrinsically stronger bond for BZY20, and (2) the processing method with larger BCZYYb7111 grains and different crack propagation, associated with the extrinsic contribution.

In addition to the difference in the average value of the fracture stress, a different data scattering can be observed, which is expected to be influenced by their sensitivity to porosity and fracture mechanisms. BCZYYb7111, with a higher grain-to-pore size ratio (r/R) and more uniform pore distribution, is less affected by pores acting as critical flaws, resulting in more consistent fracture behavior. In contrast, BZY20, with finer grains and a more heterogeneous defect distribution, is more sensitive to pore-induced stress concentration, leading to greater variability in fracture stress [48]. This is further amplified by its mixed intergranular–intragranular fracture mode, which introduces multiple crack propagation paths, whereas BCZYYb7111 exhibits more stable and uniform crack propagation.

These results establish a groundwork for further discussing how manufacturing approaches influence the mechanical reliability of proton-conducting perovskites as also discussed and assessed in the following paragraphs.

3.3.2. *Pristine vs hydrated BZY20*

The Weibull distributions of pristine and hydrated BZY20 are represented and compared in Fig. 4 with shape parameters of 2.35 and 1.95, while scale parameters of 63.02 and 38.93, respectively. The average values and standard deviations for the fracture stresses in pristine and hydrated conditions are 76.4 ± 25.9 MPa and 59.9 ± 18.7 MPa, respectively, corresponding to a decrease of approximately 22%.

Four-point bending measurements on BZY20 show a reduction in fracture stress upon hydration, which seems to disagree with most of the results found in literature, as already presented in Section 1.1, especially when partial hydration was reached. In the present study, the hydration protocol was designed to allow for complete hydration, which removes such beneficial ionic and stress gradients and instead results in a net degradation of mechanical performance. The fracture surfaces, shown in Supplementary Information in Fig. S2, highlight an increase in the intergranular propagation after hydration compared to pristine condition. This may be attributed to strengthened grain boundaries through hydroxide incorporation into oxygen vacancies, restoring lattice connectivity and strengthening grain boundaries, promoting a shift toward the intragranular crack propagation [17] and reducing the crack-wake shielding, such as bridging and deflection [45]. The crystalline structure was reported to remain cubic [37], the decrease in fracture stress is supposed to be associated with lattice expansion and bond strength variations induced by hydroxide incorporation in addition to the change in bridging effect. As already described in Section 3.2, this can weaken B–O interactions despite filling oxygen vacancies. Overall, these results indicate that hydration in BZY initially stabilizes the structure by filling oxygen vacancies due to the production of hydroxide ions [13]. At the same time, though, an extended hydration and lattice expansion weaken bond strength and reduce mechanical robustness. The fracture response, though, shows strong dependence on the hydration state (partial vs full) and the resulting distribution of residual stresses within the ceramic, as also highlighted from literature.

3.3.3. *Pristine vs hydrated BCZYYb*

The Weibull distributions of pristine and hydrated BCZYYb7111 are shown in Fig. 5, with shape parameters of 2.27 and 3.09, and scale parameters of 22.66 and 32.96, respectively. The average values and standard deviations for the fracture stresses in pristine and hydrated

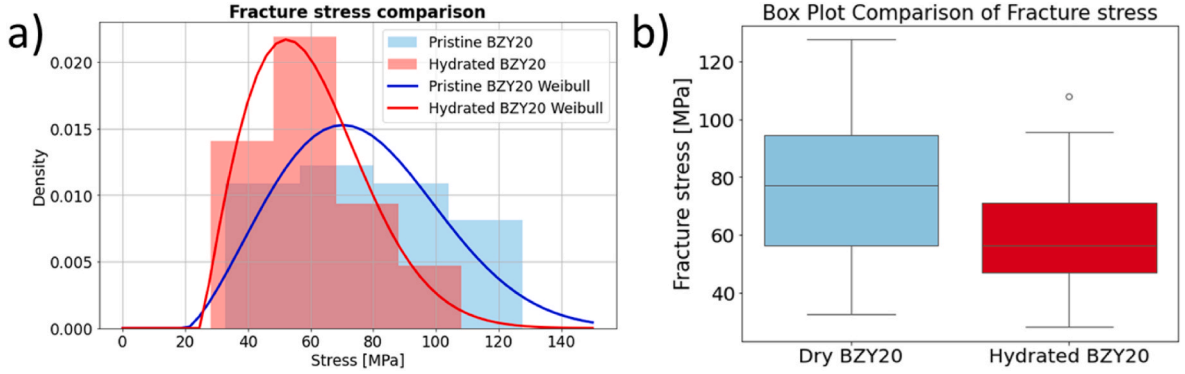

Fig. 4. (a) Weibull distribution and (b) Box Plot of Pristine and hydrated BZY20.

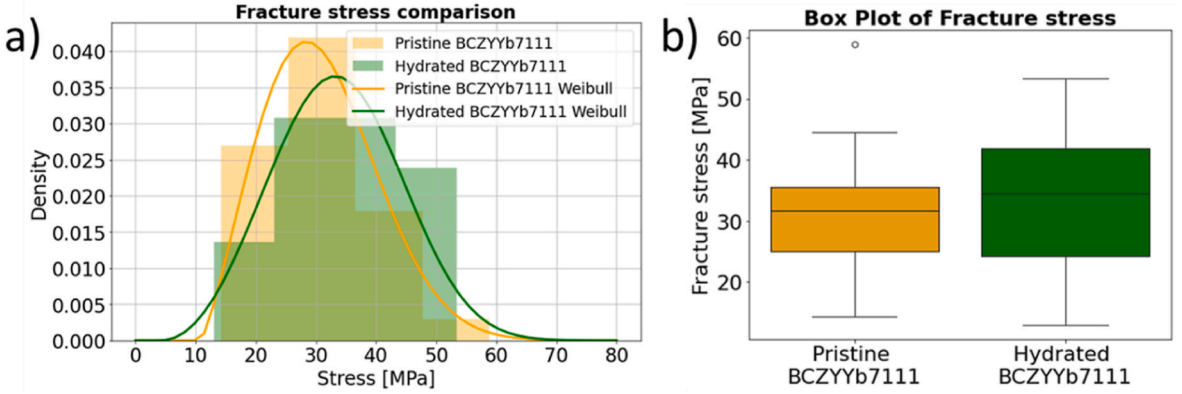

Fig. 5. (a) Weibull distribution and (b) Box Plot of Pristine and Hydrated BCZYYb7111.

conditions are 31.0 ± 9.5 MPa and 33.6 ± 10.9 MPa, respectively.

The first observation highlights the opposite effect of hydration, both compared to BZY20 and to the elastic modulus. In this scenario, the hydration is shown to improve the mechanical strength. It should be noted that, also since the starting values are already not that high, the variation is only equal to approximately +8.5%

In addition to the explanations provided in the previous paragraphs, especially regarding microscopic effects of hydration, a more detailed description of the macroscopic phenomena, especially linked to the change from intergranular to intragranular fracture, shown in the Supplementary Information in Fig. S3, occurring is provided in the fracture toughness section.

3.3.4. Overall comparison

Fig. 6 summarizes all the fracture stresses Weibull distributions and average values for easier and more complete representation. The outcomes on the fracture stresses can be highlighted.

Among the analyzed specimens, the dry BZY20 sample exhibited the best overall mechanical performance, ranking as the most reliable of the measured materials. In contrast, the dry BCZYYb7111 sample displayed the lowest fracture stress, indicating a comparatively weaker mechanical resistance. Furthermore, BZY20 and BCZYYb7111 exhibited distinct behaviors under dry and hydrated conditions, suggesting that hydration differentially affects their structural integrity and fracture mechanisms.

Overall, these findings suggest that both compositions can meet the mechanical requirements for electrolyte applications, provided that processing yields a dense, uniform, and crack-free microstructure [49].

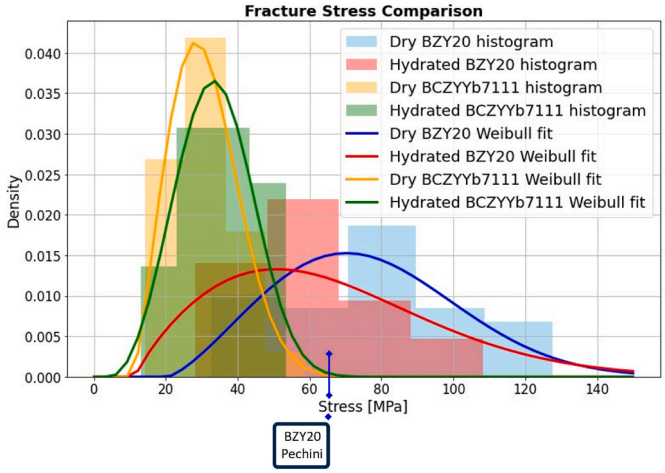

Fig. 6. Fracture stresses overall comparison.

3.4. Fracture toughness

This parameter is an intrinsic property that reflects the material's resistance to crack propagation, independent of external flaw size or geometry of a material's resistance to fracture when a stress concentrating defect is present in the sample, which is important for materials since it is nearly impossible to manufacture objects without defects [34].

A flaw of known size was manually induced in the samples, allowing for a reduction of one of the uncertainties introduced already in Section 3.3. Furthermore, this property is employed in this work to further separate between the intrinsic toughness, already discussed previously and mainly governed by covalent or equivalent bond strength, and the extrinsic contributions [50].

Some of the variability is still due to different porosities, which, though, don't show high variability as highlighted afterward in Fig. 8-b.

The fracture toughness results further reinforce the mechanical trends observed from nanoindentation and four-point bending. As shown in Fig. 7, BZY20 exhibits superior resistance to crack propagation, except for the state-of-the-art 8YSZ. This resistance decreases only slightly after hydration, with an average variation of around 4%. In contrast, BCZYYb7111 displays substantially lower fracture toughness, with average values increasing only slightly, approximately of 9%, when hydrated. In addition to the box plots shown in Fig. 7, numerical values for averages and standard deviations are also summarized in Table 3.

The corresponding critical energy release rates, calculated through the following equation

$$G_{I_c} = \frac{K_{I_c}^2}{E} \tag{5}$$

for pristine and hydrated BZY20 and BCZYYb7111, confirm that zirconium-rich compositions possess higher fracture energy and overall

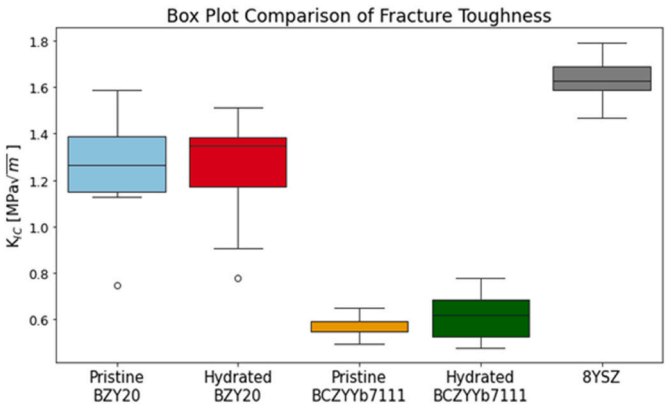

Fig. 7. Box plots for fracture toughness.

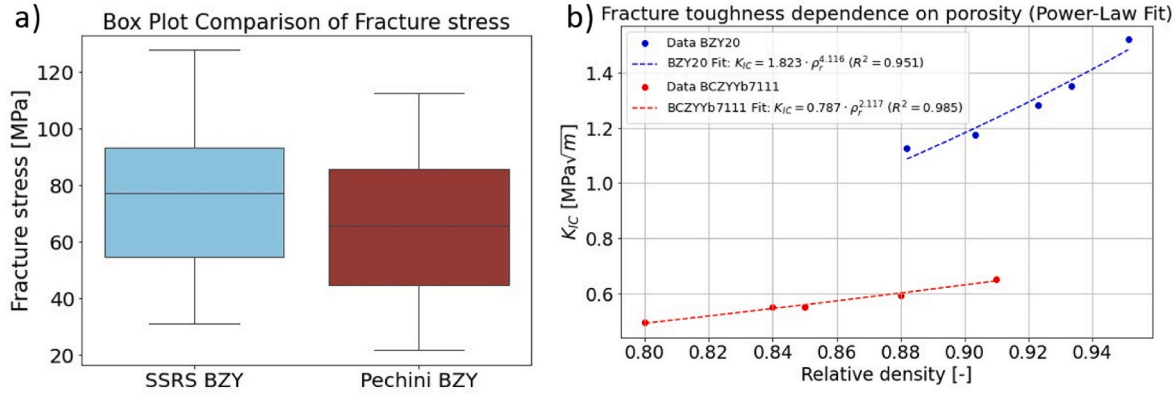

Fig. 8. Effect of manufacturing process (a) SSRS vs single phase powder (b) Dry pressing and shorter sintering for BZY20 and BCZYYb7111 respectively.

Table 3
Fracture toughness for pristine and hydrated samples.

Case Study	Fracture toughness [MPa $\sqrt{m}$]
Pristine BZY	1.32 ± 0.17
Hydrated BZY	1.33 ± 0.17
Pristine BCZYYb	0.56 ± 0.05
Hydrated BCZYYb	0.61 ± 0.11
8YSZ (literature)	1.61 ± 0.09

damage tolerance.

Critical energy release rates are summarized in Table 4.

The microstructural observations of several samples indicate that fracture in dry BZY20 occurs primarily as a combination of intragranular and intergranular pathways as shown in the supplementary information in Fig. S2, favored by the presence of residual pores and grain-boundary defects typical of solid-state reactive sintering. The effect of the hydration, on a relative and absolute point of view, agrees with the results already derived from the prior section and from what was found in literature, further confirming and validating the explanations previously provided.

Conversely, in BCZYYb7111, hydration yields a strengthening of the material, confirming what was obtained in Section 3.3 even when uncertainties related to the flaw size are removed. Some of the microscopic effects taking place during the hydration process have already been described in Section 3.2. The filling of oxygen vacancies through hydration with variation in bond strength and length, is expected to influence the local lattice distortion of orthorhombic perovskite lattice BCZYYb7111 [51] also due to enhanced tilting of BO_6 octahedra [33,35]. However, the effects on mechanical properties are not straightforward. On one hand, vacancy filling and local bonding rearrangement can enhance intrinsic lattice cohesion, potentially increasing fracture stress and toughness. On the other hand, hydration-induced chemical strain and structural distortion may counterbalance this effect. Indeed, hydration in proton-conducting perovskites is not limited to isotropic lattice expansion but also involves anisotropic strain and distortion, particularly in noncubic structures [35,51]. Consequently, hydration does not necessarily reduce structural asymmetry; instead, it may preserve or even enhance local distortions through mechanisms such as octahedral tilting and bond rearrangement. Similar hydration-driven structural modifications and lattice expansion have been reported for BCZYYb7111, highlighting the strong coupling between proton incorporation, crystal structure, and the resulting material properties [35] [52].

Table 4
Critical energy release rate for pristine and hydrated samples.

Case Study	Critical energy release rate [J/m^2]
Pristine BZY	7.2
Hydrated BZY	6.4
Pristine BCZYYb	2.3
Hydrated BCZYYb	2.9
8YSZ	12.4

From a macroscopic point of view, another common effect described in literature for brittle materials is the toughening by grain bridging [50,53] associated to the shift from intragranular to intergranular fracture. The grain bridging process can be partitioned into the five regimes of propagate, kink, arrest, stall, and bridge and to reach this final step, higher driving forces (J) are required, with normalized driving, compared to the one to propagate ($J_{0,gb}$) up to values of 7.

It is also interesting to highlight from Fig. S5–a in the Supplementary information, that even after a drying step, carried out with the same rates and dwell as the hydration process but in dry N_2 atmosphere, the fracture surface still shows intragranular fracture. At the same time, when the same thermal cycle as the hydration one is performed, but flowing continuously dry N_2, no change in the fracture surface can be observed as shown in Fig. S5–b, confirming the cause being associated with the water and not simply with the temperature change.

3.5. *Effect of manufacturing approach*

Focusing on the samples' manufacturing effects, Fig. 8 compares.

- BZY20 bars prepared by SSRS and Pechini sol-gel method,
- Effect of porosity from manufacturing on BZY20 and BCZYYb7111.

The box plots for BZY20 Pechini show similar deviation with a lower median value, as well as showing lower average values, respectively equal to 76.4 ± 25.9 and 65.9 ± 33.0 A two-tailed, independent-samples *t*-test ($\alpha = 0.05$) was also used to evaluate whether the mean values differed between the two conditions. The resulting p-value <0.05 allows rejection of the null hypothesis of equal means, supporting a statistically significant decrease in the BZY20 Pechini values.

Fig. 8-a shows the difference between SSRS and single-phase BZY20 powder. This can be attributed to the combination of phase formation, densification, and grain growth processes with highly negative Gibbs free energy for densification and possible evolution of eutectic mixture from the multiphase compacts with transient liquid phase formation [44].

The last part of the study focuses on the aspects related to the effect of porosity. The effect of grain size is not specifically studied here since all samples show approximately the same values, about 6 μm for BZY20 and 60 μm for BCZYYb7111. For each sample used to study the fracture toughness, the porosity and relative densities have been extracted using ImageJ software, and a regression has been calculated according to a power law [54]. In addition to the different absolute K_{IC} values, the two

materials show a different porosity sensitivity, as indicated by the different slopes. Literature relates the normalized toughness to the grain-to-pore size ratio (r/R), which increases as r/R increases since pores become less effective and more impactful.

In our case, BCZYYb7111 is less sensitive to porosity because it shows smaller pores, likely due to finer starting powder and a more uniform distribution of organics and a larger grain size, leading to a higher effective r/R and thus a reduced porosity effect compared to BZY20 [48].

4. Conclusions

This study provides the first comprehensive assessment of the mechanical properties of protonic ceramics BZY20 and BCZYYb7111, both in pristine and fully hydrated states. It bridges the gaps in the literature regarding statistical reliability, through the study of at least 150 samples, and test protocols used for testing and hydration. The results highlight the markedly different mechanical properties of proton-conducting perovskites. Several factors have been emphasized, including their chemistry, crystal symmetry, crystal structure, porosity, and grain size.

This study has identified that BZY20, due to the presence of zirconium, exhibits superior mechanical performance for all the evaluated properties. In addition to the bond differences, microstructure, manufacturing-generated defects, and manufacturing routes (Solid-State Reactive Sintering vs conventional sintering) also affect the mechanical properties. Hydration was shown to weaken BZY20 mechanical properties due to lattice expansion and bond strain, and a slight reduction of intragranular fracture, resulting in a fracture stress and toughness reduction. BCZYYb7111 shows, instead, an improvement post hydration, mostly linked to the orthorhombic structure and the change from inter to intragranular fracture, taking advantage of grain bridging.

Compared to the more standardized 8YSZ, BZY20 demonstrates promising robustness, making it a strong candidate for scaling up in protonic ceramic fuel cells and electrolyzers. However, BCZYYb7111's hydration-induced toughening suggests potential for optimization and material engineering.

According to these observations, obtaining a mechanically strong material requires a combination of compositional and microstructural control. First, a high-zirconium-content perovskite is beneficial, as it enhances bond strength and elastic stiffness. Second, controlled doping should be employed to minimize lattice strain and avoid excessive structural distortion. From a processing perspective, achieving a fine, homogeneous microstructure with low porosity is essential to improve strength. Finally, grain boundaries can be engineered to promote crack deflection and grain bridging, thereby enhancing the effective fracture resistance. Coupling all these properties would unify the intrinsic stiffness of BZY20 with the toughening mechanisms observed in hydrated BCZYYb7111, yielding the highest possible mechanical resilience for proton-conducting ceramics. In particular, if a fully dense, homogeneous, and defect-free electrolyte with an optimized microstructure is obtained, the mechanical properties are expected to be sufficient to resist to the internal stresses arising from thermal and chemical expansion in normal operating conditions. It should also be noted that, although this study is especially valid when electrolyte-supported cells are used, the findings of this research provide insights also for negatrode-supported cells, further strengthening the results and conclusions of this work.

Abbreviations

ASTM	American Society for Testing and Materials
BCY	Yttrium-doped barium cerate
BCZYYb7111	BaCe0.7Zr0.1Y0.1O3-δ
BKCZY	Ba1-xKxCe0.6Zr0.2Y0.2O3-δ
BoP	Balance of Plant
BZCY721	BaCe0.20Zr0.70Y0.10O3-δ
BZY	Yttrium-doped barium zirconate
BZY20	BaZr0.8Y0.2O3-δ
EDTA	Ethylenediaminetetraacetic Acid
GDC	Gadolinium-doped ceria
G_{IC}	Energy release rate
ISO	International Organization for Standardization
J	Driving force
K_{IC}	Fracture toughness
NiO	Nickel Oxide
PCCs	Protonic ceramic cells
PVA	Polyvinyl Alcohol
RES	Renewable energy sources
SEM	Scanning Electron Microscope
SEVNB	Single Edge V-Notched Beam
SSRS	Solid-state reactive sintering
XRD	X-ray powder diffraction
YSZ	Yttria-stabilized zirconia
ZDC	Zr-doped ceria

CRediT authorship contribution statement

Andrea Moranti: Formal analysis, Investigation, Methodology, Visualization, Writing – original draft, Writing – review & editing. **Sandrine Ricote:** Methodology, Supervision, Writing – review & editing. **Federico Smeacetto:** Funding acquisition, Supervision, Writing – review & editing. **Massimo Santarelli:** Funding acquisition, Supervision, Writing – review & editing.

Declaration of competing interest

The authors declare the following financial interests/personal relationships which may be considered as potential competing interests: Andrea Moranti reports financial support was provided by Bruno Kessler Foundation. If there are other authors, they declare that they have no known competing financial interests or personal relationships that could have appeared to influence the work reported in this paper.

Acknowledgement

The authors are particularly grateful to Ivar Reimanis and Ryan McGinnis from the Colorado School of Mines for their support. Special regards also go to the contributions of colleagues and technical staff who assisted with this work. The authors also would like to acknowledge Fondazione Bruno Kessler (FBK) for funding Andrea Moranti's PhD, which contributed to this publication.

Appendix A. Supplementary data

Supplementary data to this article can be found online at https://doi.org/10.1016/j.jpowsour.2026.240503.

Data availability

Data will be made available on request.

References

[1] M.F. Lagadec, A. Grimaud, Water electrolysers with closed and open electrochemical systems, Nat. Mater. 19 (2020) 1140–1150, https://doi.org/10.1038/s41563-020-0788-3.
[2] I.T. Bello, S. Zhai, Q. He, C. Cheng, Y. Dai, B. Chen, et al., Materials development and prospective for protonic ceramic fuel cells, Int. J. Energy Res. 46 (2022) 2212–2240, https://doi.org/10.1002/er.7371.
[3] K.-D. Kreuer, Proton-conducting oxides, Annu. Rev. Mater. Res. 33 (2003) 333–359, https://doi.org/10.1146/annurev.matsci.33.022802.091825.

[4] A. Løken, S. Ricote, S. Wachowski, Thermal and chemical expansion in proton ceramic electrolytes and compatible electrodes, Crystals 8 (2018), https://doi.org/10.3390/cryst8090365.

[5] N.A. Danilov, I.A. Starostina, G.N. Starostin, A.V. Kasyanova, D.A. Medvedev, Z. Shao, Fundamental understanding and applications of protonic Y- and Yb-Coped Ba(Ce,Zr)O3 perovskites: State-of-the-Art and perspectives, Adv. Energy Mater. 13 (2023) 2302175, https://doi.org/10.1002/aenm.202302175.

[6] S. Choi, C.J. Kucharczyk, Y. Liang, X. Zhang, I. Takeuchi, H.-I. Ji, et al., Exceptional power density and stability at intermediate temperatures in protonic ceramic fuel cells, Nat. Energy 3 (2018) 202–210, https://doi.org/10.1038/s41560-017-0085-9.

[7] Z. Luo, X. Hu, Y. Zhou, Y. Ding, W. Zhang, T. Li, et al., Harnessing high-throughput computational methods to accelerate the discovery of optimal proton conductors for high-performance and durable protonic ceramic electrochemical cells, Adv. Mater. 36 (2024) 2311159, https://doi.org/10.1002/adma.202311159.

[8] N.A. Danilov, I.A. Starostina, G.N. Starostin, A.V. Kasyanova, D.A. Medvedev, Z. Shao, Fundamental understanding and applications of protonic Y-and Yb-coped Ba (Ce, Zr) O3 perovskites: state-of-the-art and perspectives, Adv. Energy Mater. 13 (2023) 2302175, https://doi.org/10.1002/aenm.202302175.

[9] L.Q. Le, C.H. Hernandez, M.H. Rodriguez, L. Zhu, C. Duan, H. Ding, et al., Proton-conducting ceramic fuel cells: scale up and stack integration, J. Power Sources 482 (2021) 228868, https://doi.org/10.1016/j.jpowsour.2020.228868.

[10] A. Moranti, J. Dailly, M. Santarelli, F. Smeacetto, Techno-economic analysis on proton conductor ceramic based technologies for various materials, configurations, applications and products, Energy Convers. Manag. 321 (2024) 119082, https://doi.org/10.1016/j.enconman.2024.119082.

[11] D. Vignesh, E. Rout, Technological challenges and advancement in proton conductors: a review, Energy & Fuels 37 (2023) 3428–3469, https://doi.org/10.1021/acs.energyfuels.2c03926.

[12] E. Mercadelli, A. Gondolini, M. Ardit, G. Cruciani, C. Melandri, S. Escolastico, et al., Chemical and mechanical stability of BCZY-GDC membranes for hydrogen separation, Sep. Purif. Technol. 289 (2022) 120795, https://doi.org/10.1016/j.seppur.2022.120795.

[13] E. Makagon, R. Merkle, J. Maier, I. Lubomirsky, Influence of hydration and dopant ionic radius on the elastic properties of BaZrO3, Solid State Ion 344 (2020) 115130, https://doi.org/10.1016/j.ssi.2019.115130.

[14] P.-F. Yang, D.-L. Chen, S.-R. Jian, S.-W. Lee, C.-J. Tseng, Mechanical properties of Ba1-xKxCe0. 6Zr0. 2Y0. 2O3-δ oxides by nanoindentation, Procedia Eng. 79 (2014) 599–605, https://doi.org/10.1016/j.proeng.2014.06.385.

[15] Z. Wang, Y. Jing, Y. Sun, W. Li, J. Yang, X. Li, Hydration induced mechanical degradation in the Y-doped BaZrO3 solid oxide, Comput. Mater. Sci. 235 (2024) 112824, https://doi.org/10.1016/j.commatsci.2024.112824.

[16] T. Ueno, W. Miyamoto, S. Kondo, T. Teranishi, A. Kishimoto, Temporary reinforcement of proton-conductive ceramics by introducing a graded carrier, Mater. Sci. Eng., B 321 (2025) 118499, https://doi.org/10.1016/j.mseb.2025.118499.

[17] R. Sažinas, M.-A. Einarsrud, T. Grande, Toughening of Y-doped BaZrO 3 proton conducting electrolytes by hydration, J Mater Chem A Mater 5 (2017) 5846–5857, https://doi.org/10.1039/C6TA11022C.

[18] B.L. Kee, PROTONIC CERAMICS FOR ELECTROCHEMICAL HYDROGEN COMPRESSION, 2020.

[19] W. Tang, W. Bian, H. Ding, Y. Ding, Z. Zhao, Q. Sun, et al., Sintering protonic zirconate cells with enhanced electrolysis stability and faradaic efficiency, Nat. Synth. 4 (2025) 592–602, https://doi.org/10.1038/s44160-025-00765-z.

[20] H. Zhu, Y. Shin, S. Ricote, R.J. Kee, Thermodynamics, transport, and kinetics in BaZr0.8Y0.2O3−δ electrolytes and their impact on hydrogen separation and compression, J. Electrochem. Soc. 170 (2023) 64501, https://doi.org/10.1149/1945-7111/acd8f6.

[21] D. Han, K. Toyoura, T. Uda, Protonated BaZr0.8Y0.2O3−δ: impact of hydration on electrochemical conductivity and local crystal structure, ACS Appl. Energy Mater. 4 (2021) 1666–1676, https://doi.org/10.1021/acsaem.0c02832.

[22] S. Watanabe, K. Sato, F. Iguchi, K. Yashiro, T. Hashida, T. Kawada, Mechanical strength evaluation of YSZ, GDC and LSCF under SOFC operating conditions, ECS Trans. 78 (2017) 2181, https://doi.org/10.1149/07801.2181ecst.

[23] M. Ghatee, M.H. Shariat, J.T.S. Irvine, Investigation of electrical and mechanical properties of 3YSZ/8YSZ composite electrolytes, Solid State Ion 180 (2009) 57–62, https://doi.org/10.1016/j.ssi.2008.10.006.

[24] L. Donzel, S.G. Roberts, Microstructure and mechanical properties of cubic zirconia (8YSZ)/SiC nanocomposites, J. Eur. Ceram. Soc. 20 (2000) 2457–2462, https://doi.org/10.1016/S0955-2219(00)00117-5.

[25] Y. Li, H. Sun, J. Song, Z. Zhang, H. Lan, L. Tian, et al., Effect of two-step sintering on the mechanical and electrical properties of 5YSZ and 8YSZ ceramics, Materials 16 (2023) 2019, https://doi.org/10.3390/ma16052019.

[26] R. Maurya, A. Gupta, S. Omar, K. Balani, Effect of sintering on mechanical properties of ceria reinforced yttria stabilized zirconia, Ceram. Int. 42 (2016) 11393–11403, https://doi.org/10.1016/j.ceramint.2016.04.069.

[27] T. Fujimoto, V. Seriacopi, L. Ferreira, I. Machado, E. Muccillo, Mechanical and electrical characterization of 8YSZ-ScCeSZ ceramics, Mater. Res. 26 (2023) e20220595, https://doi.org/10.1590/1980-5373-MR-2022-0595.

[28] B. Aktas, S. Tekeli, Effect of Co_3O_4 on the fracture toughness and microstructure of Yttria-Stabilized Cubic Zirconia (8YSZ), Acta Phys Pol A 127 (2015) 1384–1387, https://doi.org/10.12693/APhysPolA.127.1384.

[29] M. Morales, J.J. Roa, X.G. Capdevila, M. Segarra, S. Piñol, Mechanical properties at the nanometer scale of GDC and YSZ used as electrolytes for solid oxide fuel cells, Acta Mater. 58 (2010) 2504–2509, https://doi.org/10.1016/j.actamat.2009.12.036.

[30] H. Liu, W. Zhao, Y. Ji, J. Cui, Y. Chu, P. Rao, Determination of fracture toughness of zirconia ceramics with different yttria concentrations by SEVNB method, Ceram. Int. 43 (2017) 10572–10575, https://doi.org/10.1016/j.ceramint.2017.04.064.

[31] X. Ren, W. Pan, Mechanical properties of high-temperature-degraded yttria-stabilized zirconia, Acta Mater. 69 (2014) 397–406, https://doi.org/10.1016/j.actamat.2014.01.017.

[32] S. Ricote, N. Bonanos, A. Manerbino, W.G. Coors, Conductivity study of dense BaCexZr(0.9−x)Y0.1O(3−δ) prepared by solid state reactive sintering at 1500 °C, Int. J. Hydrogen Energy 37 (2012) 7954–7961, https://doi.org/10.1016/j.ijhydene.2011.08.118.

[33] L. Hamze, O. Joubert, E. Quarez, Phase diagrams and chemical expansion upon hydration of proton conductors BaZrxCe0.8−xY0.1Yb0.1O2.9(H2O)n ($0 \leq x \leq 0.8$; $0 \leq n \leq 0.1$), J. Mater. Chem. A 14 (2026) 1584–1600, https://doi.org/10.1039/D5TA07218B.

[34] W.D. Callister, Materials Science and Engineering: an Introduction, 1985.

[35] K. Nomura, H. Shimada, Y. Yamaguchi, W. Shin, Y. Okuyama, Y. Mizutani, Phase transitions, thermal expansions, chemical expansions, and CO2 resistances of Ba (Ce0.8-xZrxY0.1Yb0.1)O3-δ (x = 0.1, 0.4) perovskite-type proton conductors, J. Electrochem. Soc. 169 (2022) 024516, https://doi.org/10.1149/1945-7111/ac5480.

[36] L. Pauling, The Nature of the Chemical Bond and the Structure of Molecules and Crystals, Cornell University Press, 1960.

[37] A.K.E. Andersson, S.M. Selbach, C.S. Knee, T. Grande, Chemical expansion due to hydration of proton-conducting perovskite oxide ceramics, J. Am. Ceram. Soc. 97 (2014) 2654–2661, https://doi.org/10.1111/jace.12990.

[38] Y. Zhang, D. Xie, B. Chi, J. Pu, J. Li, D. Yan, Basic properties of proton conductor BaZr0.1Ce0.7Y0.1Yb0.1O3-δ (BZCYYb) material, Asia Pac. J. Chem. Eng. 14 (2019) e2322, https://doi.org/10.1002/apj.2322.

[39] Materials project (n.d.) Next-Gen Materials Project. Retrieved January 12, 2026, from https://next-gen.materialsproject.org/materials.

[40] T. Chen, Y. Jing, L.O. Anderson, K. Leonard, H. Matsumoto, N. Aluru, et al., Toward durable protonic ceramic cells: Hydration-induced chemical expansion correlates with symmetry in the Y-Doped BaZrO3–BaCeO3 solid solution, J. Phys. Chem. C 125 (2021) 26216–26228, https://doi.org/10.1021/acs.jpcc.1c08334.

[41] Z. Qiao, S. Li, Y. Li, N. Xu, K. Xiang, Structure, mechanical properties, and thermal conductivity of BaZrO3 doped at the A-B site, Ceram. Int. 48 (2022) 12529–12536, https://doi.org/10.1016/j.ceramint.2022.01.120.

[42] X. Tan, Z. Shen, A. Bokhari, W. Ali, N. Han, Effect of Co2O3 as sintering aid on perovskite BaCe0.8Y0.2O3-δ proton conductive membrane for hydrogen separation, Int. J. Hydrogen Energy 48 (2023) 26551–26558, https://doi.org/10.1016/j.ijhydene.2022.11.165.

[43] D. Ciria, M. Ben Hassine, M. Jiménez-Melendo, A. Iakovleva, P. Haghi-Ashtiani, V. Aubin, et al., Mechanical degradation under hydrogen of yttrium doped barium zirconate electrolyte material prepared with NiO additive, J. Power Sources 321 (2016) 226–232, https://doi.org/10.1016/j.jpowsour.2016.05.001.

[44] S. Nikodemski, J. Tong, R. O'Hayre, Solid-state reactive sintering mechanism for proton conducting ceramics, Solid State Ion 253 (2013) 201–210, https://doi.org/10.1016/j.ssi.2013.09.025.

[45] R.W. Rice, Grain size and porosity dependence of ceramic fracture energy and toughness at 22 C, J. Mater. Sci. 31 (1996) 1969–1983.

[46] E. Novitskaya, K. Karandikar, K. Cummings, M. Mecartney, O.A. Graeve, Hall–petch effect in binary and ternary alumina/zirconia/spinel composites, J. Mater. Res. Technol. 11 (2021) 823–832.

[47] A. Phatak, P. Gupta, S. Mandal, H. Agrawal, O. Parkash, D. Kumar, Hardness-porosity-grain size interrelationship in conventionally sintered 3 mol% yttria stabilized zirconia, High-Temperature Materials 1 (2024).

[48] C. Lu, R. Danzer, F.D. Fischer, Scaling of fracture strength in ZnO: effects of pore/grain-size interaction and porosity, J. Eur. Ceram. Soc. 24 (2004) 3643–3651, https://doi.org/10.1016/j.jeurceramsoc.2003.12.001.

[49] A. Dubois, K. Taghikhani, J.R. Berger, H. Zhu, R.P. O'Hayre, R.J. Braun, et al., Chemo-thermo-mechanical coupling in protonic ceramic fuel cells from fabrication to operation, J. Electrochem. Soc. 166 (al) (2019) F1007, https://doi.org/10.1149/2.1071912jes.

[50] R.O. Ritchie, Toughening materials: enhancing resistance to fracture, Philos. Trans. R. Soc. A Math. Phys. Eng. Sci. 379 (2021), https://doi.org/10.1098/rsta.2020.0437.

[51] N.T.Q. Nguyen, H.H. Yoon, Preparation and evaluation of BaZr0.1Ce0.7Y0.1Yb0.1O3−δ (BZCYYb) electrolyte and BZCYYb-based solid oxide fuel cells, J. Power Sources 231 (2013) 213–218, https://doi.org/10.1016/j.jpowsour.2013.01.011.

[52] T. Chen, Y. Jing, L.O. Anderson, K. Leonard, H. Matsumoto, N. Aluru, et al., Toward durable protonic ceramic cells: hydration-induced chemical expansion correlates with symmetry in the Y-Doped BaZrO3–BaCeO3 solid solution, J. Phys. Chem. C 125 (2021) 26216–26228, https://doi.org/10.1021/acs.jpcc.1c08334.

[53] I.I.I.J.W. Foulk, G.C. Johnson, P.A. Klein, R.O. Ritchie, On the toughening of brittle materials by grain bridging: promoting intergranular fracture through grain angle, strength, and toughness, J Mech Phys Solids 56 (2008) 2381–2400, https://doi.org/10.1016/j.jmps.2007.12.006.

[54] D.E. Dunn, L.J. LaFountain, R.E. Jackson, Porosity dependence and mechanism of brittle fracture in sandstones, J. Geophys. Res. 78 (1973) 2403–2417, https://doi.org/10.1029/JB078i014p02403.